Kinetic magnetization by fast electrons in laser-produced plasmas at sub-relativistic intensities

Kinetic magnetization by fast electrons in laser-produced plasmas at sub-relativistic intensities

Tadeusz Pisarczyk, Sergey Yu. Gus'kov, Tomasz Chodukowski, Roman Dudzak, Philipp Korneev, Nicolai N. Demchenko, Zofia Kalinowska, Jan Dostal, Agnieszka Zaras-Szydlowska, Stefan Borodziuk, Libor Juha, Jakub Cikhardt, Josef Krasa, Daniel Klir, Balzhima Cikhardtova, Pavel Kubes, Eduard Krousky, Miroslav Krus, Jiri Ullschmied, Karel Jungwirth, Jan Hrebicek, Tomas Medrik, Jiri Golasowski, Miroslav Pfeifer, Oldrich Renner, Sushil Singh, Satyabrata Kar, Hamad Ahmed, Jiri Skala, and Pawel Pisarczyk

Citation: Physics of Plasmas **24**, 102711 (2017);

View online: https://doi.org/10.1063/1.4995044

View Table of Contents: http://aip.scitation.org/toc/php/24/10

Published by the American Institute of Physics

Kinetic magnetization by fast electrons in laser-produced plasmas at sub-relativistic intensities

Tadeusz Pisarczyk,[1,a)] Sergey Yu. Gus'kov,[2,3] Tomasz Chodukowski,[1] Roman Dudzak,[4,5] Philipp Korneev,[2,3] Nicolai N. Demchenko,[2] Zofia Kalinowska,[1] Jan Dostal,[4,5] Agnieszka Zaras-Szydlowska,[1] Stefan Borodziuk,[1] Libor Juha,[4,5] Jakub Cikhardt,[5,6] Josef Krasa,[4] Daniel Klir,[5,6] Balzhima Cikhardtova,[6] Pavel Kubes,[6] Eduard Krousky,[5] Miroslav Krus,[4,5] Jiri Ullschmied,[5] Karel Jungwirth,[4] Jan Hrebicek,[4,5] Tomas Medrik,[4,5] Jiri Golasowski,[4,5] Miroslav Pfeifer,[4,5] Oldrich Renner,[4,5] Sushil Singh,[4] Satyabrata Kar,[7] Hamad Ahmed,[7] Jiri Skala,[5] and Pawel Pisarczyk[8]

[1]*Institute of Plasma Physics and Laser Microfusion, 01-497 Warsaw, Poland*
[2]*P. N. Lebedev Physical Institute of RAS, 119991 Moscow, Russian Federation*
[3]*National Research Nuclear University MEPhI, 115409 Moscow, Russian Federation*
[4]*Institute of Physics, Czech Academy of Sciences, 182 21 Prague, Czech Republic*
[5]*Insitute of Plasma Physics, Czech Academy of Sciences, 182 00 Prague, Czech Republic*
[6]*Faculty of Electrical Engineering, Czech Technical University, 166 27 Prague, Czech Republic*
[7]*Queens University of Belfast, BT7 1NN Belfast, United Kingdom*
[8]*Warsaw University of Technology, ICS, 00-661 Warsaw, Poland*

(Received 10 July 2017; accepted 2 October 2017; published online 24 October 2017)

The problem of spontaneous magnetic field generation with nanosecond laser pulses raises a series of fundamental questions, including the intrinsic magnetization mechanisms in laser-driven plasmas and the understanding of charge-discharge processes in the irradiated target. These two issues are tightly bound as the charge-discharge processes are defined by the currents, which have in turn a feedback by magnetic fields in the plasma. Using direct polaro-interferometric measurements and theoretical analysis, we show that at parameters related to the PALS laser system (1.315 μm, 350 ps, and 10^{16} W/cm^2), fast electrons play a decisive role in the generation of magnetic fields in the laser-driven plasma. Spatial distributions of electric currents were calculated from the measured magnetic field and plasma density distributions. The obtained results revealed the characteristics of strong currents observed in capacitor-coil magnetic generation schemes and open a new approach to fundamental studies related to magnetized plasmas. https://doi.org/10.1063/1.4995044

I. INTRODUCTION

Studies of physical processes accompanying the interaction of sub-relativistic nanosecond laser pulses with dense targets started a long time ago (see, for example, books[1,2]). Nowadays, plenty of analytical models and numerical schemes are used routinely for the prediction and explanation of experimental data dealing with fast electron generation, spontaneous plasma magnetization, dense matter heating, and many other phenomena. However, a variety of the studied physical effects is very rich and some of those which emerged recently may contribute substantially to our general understanding of laser-matter interactions.

Among these, investigation of the spontaneous magnetic fields (SMFs) generated in the laser-produced plasma is a modern trend relating to a set of fundamental applications in high energy density physics. One can mention the capacitor-coil laser-driven schemes as[3] interesting, e.g., in the fast ignition concept of the inertial confinement fusion (ICF) approach;[4–7] laser-production of magnetized plasmas in shaped targets,[8,9] considered also for neutronless ICF schemes;[10] SMF-related phenomena in the dense or compressed plasma and their influence on its transport and relaxation properties, see, e.g., Ref. 11; astrophysical laboratory studies, see, e.g., Ref. 12, including well known problems of reconnection of magnetic lines and jet generation. An important question is a role of different sources of SMF generation under particular conditions of laser-matter interaction. Several of them are of paramount importance: the thermo-electric mechanism,[13–15] ponderomotive currents,[16] and laser accelerated fast electrons.[17,18] In this paper, the SMF generation is studied in a plasma produced by interaction of the beam of the iodine laser PALS with a solid target, operating in the first harmonic. In many experiments carried out with terawatt nanosecond laser pulses in the absence of the efficient fast electron generation, magnetic fields in a range of several MGs were recorded (see, e.g., review[19]). Under these conditions, the thermo-electric current corresponding to the vector product of pressure and density gradients in a plasma torch was considered as a source of SMF.

In this work, we selected the experimental conditions which permit the action of two SMF-generation mechanisms associated with both thermo-electric and fast-electron currents. We unravel the origin of the SMF via the two mentioned sources of the magnetic field by analyzing the observed SMF and density distribution at different time

[a)]tadeusz.pisarczyk@ifpilm.pl

periods of the laser-matter interaction. Although experimental measurements of the currents in the interaction region represent a quite difficult problem, the magnetic fields help us to define the integral electron currents and to compare them with prevised current of fast electrons.

To switch on the fast-electron source of the SMF, the experiments were carried out with the laser beam tightly focused into a spot with a radius of 50 μm, which provided the radiation intensity on the target of about $I \approx 10^{16}$ W/cm^2. Sharp focusing and a relatively short pulse duration provided large pressure and density gradients during the irradiation of the target. A high laser intensity and a high coupling parameter $I\lambda^2 \approx 2 \times 10^{16}$ Wμm^2/cm^2 in a combination with the relatively short size of the plasma torch correspond to absorption of a large fraction of the laser energy by the resonance mechanism and its further transformation into the energy of fast electrons. Previous experiments performed under these conditions determined the fraction of the resonantly absorbed energy up to 5% of the total laser energy, while the fast electron energy was about 100 keV.[20,21]

For the SMF measurements, we used the optical diagnostics based on the Faraday effect[22] (rotation of the polarization plane) in combination with the measurement of the electron density distribution implemented earlier on the PALS system.[23] Among many methods used for the magnetic field measurement in the laser-driven plasma, such as proton deflectometry, direct B-dot, and optical techniques, this one allows to obtain probably the most complete information about the magnetic field, in particular, its spatial and temporal distribution, though only in the transparent area of the investigated plasma. However, due to a set of technical difficulties, e.g., time gating, synchronization of the plasma producing and probing beams, plasma self-emission, etc., hitherto this method has limitedly been applied in studies of the magnetized plasmas. Recent progress achieved in synchronization of the sub-ns plasma producing beam and the probe femtosecond beam[24] provided a possibility to measure the SMF distribution in the ablative plasma with an extremely high spatial and temporal resolution.[23] Due to collection of these high quality data characterizing the SMF evolution, the understanding of its nature and origin becomes possible.

II. EXPERIMENTAL SETUP AND RESULTS

The experiments were performed on the PALS facility. The 1ω, linearly polarized single laser beam (1.315 μm) delivered with a normal incidence an energy of ≈250 J in 350 ps at a planar copper massive target, focused to a minimal focal spot radius (FWHM) $R_L = 50$ μm, which corresponds to the intensity of about 10^{16} W/cm^2. At the PALS Research Infrastructure, the Hartmann's techniques are used[25] to determine the minimal focal spot radius.

The SMF distributions were measured by means of the two-channel polaro-interferometric diagnostic system driven by the Ti:Sa laser pulse with the wavelength of 808 nm and the pulse duration of 40 fs; see Ref. 23 for more details.

The quantitative analysis of the SMF and plasma density distributions was based on polarograms and interferograms registered at different times during the expansion of the ablative plasma from the laser-irradiated target surface. The corresponding raw images are shown in Fig. 1.

Reconstruction of the SMF distributions was performed by the standard methodology described, e.g., in Ref. 23. The results of the reconstructed SMF and the plasma density distributions are shown in Figs. 2 and 3, respectively. The data corresponds to the four time moments during the plasma expansion, which are related to the maximum laser pulse intensity ($t = 0$), namely, before the maximum of the laser pulse ($t = -85$ ps), near the maximum of the laser pulse ($t = 20$ ps), after the maximum of the laser pulse ($t = 161$ ps), and at the end of the laser pulse ($t = 257$ ps).

The magnetic field distributions (Fig. 2) show that the SMF in general grows up to the front edge of the plasma. As follows from Fig. 2 for $t = 161$ ps, the maximum value (about 28 MGs) is observed on the front of the ablative plasma at the end of the laser pulse ($t = 161$ ps).

Using the measured space-time SMF distributions, we calculated the current density distributions and the SMF energy for the selected times. The additional data obtained in previous PALS experiments were attracted for the analysis, namely, the total electric currents in the target support measured in Ref. 26 and the electron spectra in the range from few hundred keV up to 3 MeV measured in Ref. 27. The latter was obtained using the spectrometer with the opening diameter of 1 mm placed at a distance of 28 cm from the target at the angle of 30° from the laser beam axis; see Ref. 27 for details.

A. Current density distributions

Based on the spatial distribution of the magnetic field, we calculated the relevant current density. Considering only the azimuthal component of the SMF $\vec{B} = (0, B_\varphi, 0)$, which is supported by the observed geometry of the interaction and antisymmetry of the raw data in Fig. 1, the current density distributions $\vec{j}(r, z)$ read by the Ampere's law:

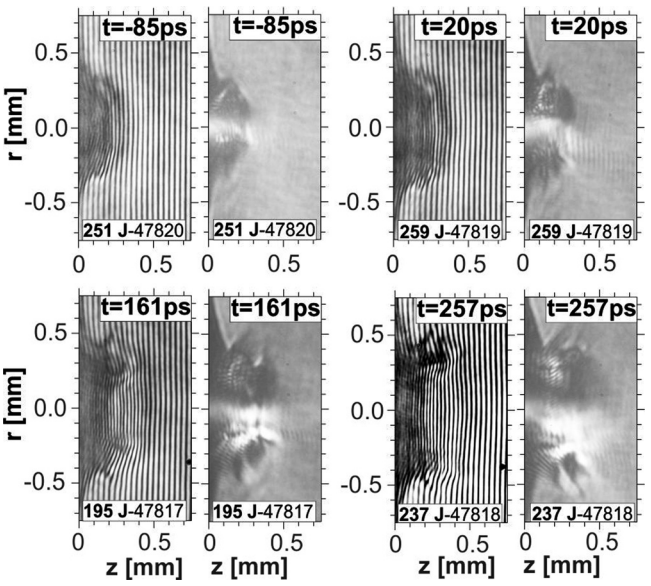

FIG. 1. Femtosecond raw interferograms (left) and polarograms (right) registered at different expansion times during the laser beam interaction with the Cu planar massive target.

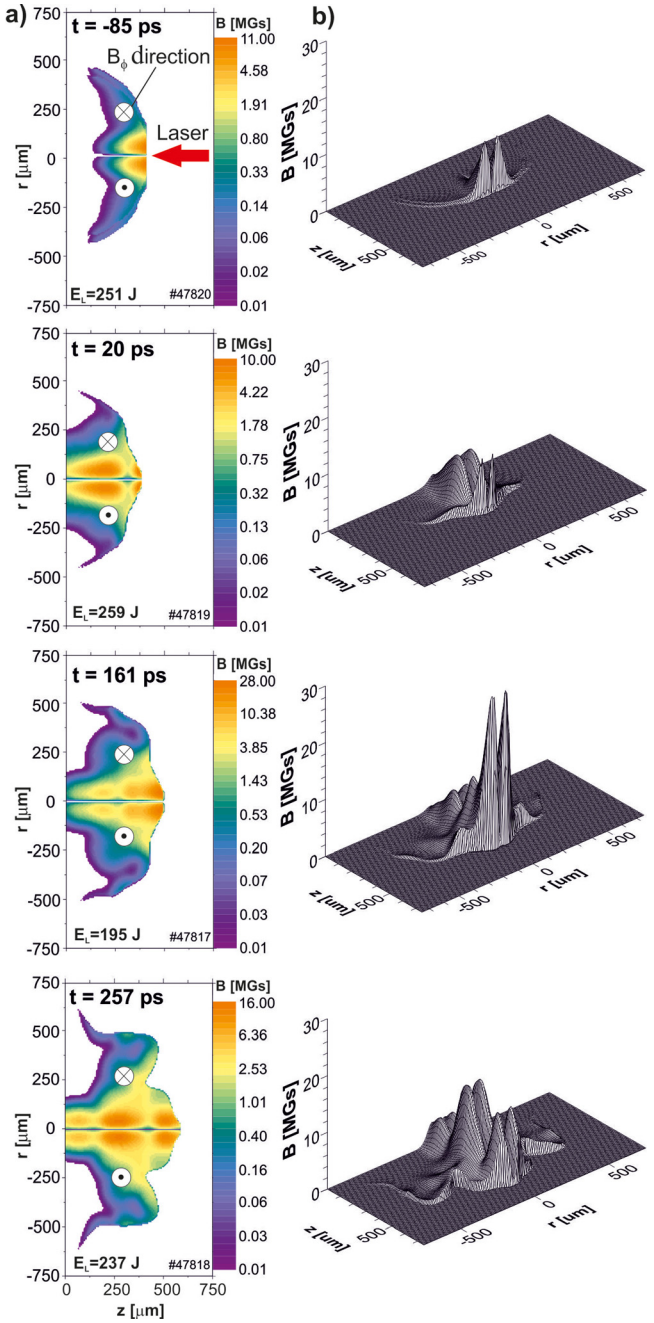

FIG. 2. The SMF distributions: (a) color-plots and (b) space profiles of the SMF during the laser pulse interaction with the Cu massive planar target. The direction of the registered magnetic field is shown on the SMF color distributions. The errors in the SMF values are about 20 %.

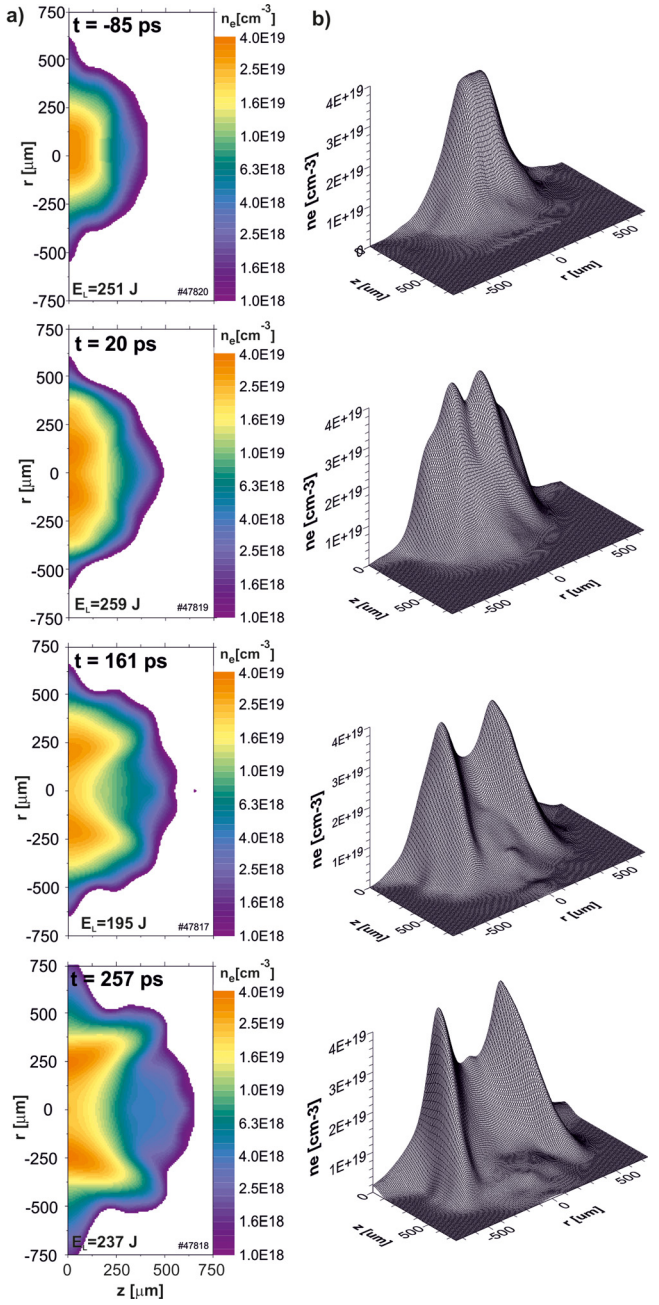

FIG. 3. The electron density distributions: (a) color-plots and (b) space profiles during the laser pulse interaction with the Cu massive planar target. The errors in the density values are about 20 %.

$$\vec{j}(r,z) = j_z(r,z)\vec{e}_z + j_r(r,z)\vec{e}_r,$$
$$= \frac{1}{\mu_0}\left[\frac{\partial B_\phi(r,z)}{\partial r} + \frac{B_\phi(r,z)}{r}\right]\vec{e}_z$$
$$+ \frac{1}{\mu_0}\left[\frac{\partial B_\phi(r,z)}{\partial z}\right]\vec{e}_r, \qquad (1)$$

where $\mu_0 = 4\pi \cdot 10^{-7}$ H/m is the vacuum permeability and $B_\phi(r,z)$ is the magnetic field distribution.

We use the cylindrical coordinate system where r is the distance from the symmetry axis. In Eq. (1), we disregard displacement currents, because the time evolution is quite slow. The calculated results are presented in Fig. 4 where we artificially separated the currents to direct with $j_z > 0$ (electrons are moving predominantly from the target) and return with $j_z < 0$ (electrons are moving predominantly toward the target). For both cases, the absolute value of the current $j = |\vec{j}|$ is shown. As follows from the direct $j(r, z)$ distributions [Fig. 4(a)], almost the whole direct current in the area available for polaro-interferometry is confined within an axial cylinder of about 130 μm in diameter. In contrary, the return current has a wide spatial spread outside this cylinder, and thus the return current density is much smaller than that of the direct current; see the color scales in Fig. 4. The evaluation of the spatial distribution of both the direct and return current densities shows a much complex structure than it was observed with the use of a wire-probe technique employed by Drouet *et al.*[28,29]

Nevertheless, there the return current distribution had a similar configuration.

To demonstrate clearly the structure of these distributions, the radial magnetic field and current density profiles in the cross-section at $z = 250\ \mu$m are shown in Fig. 5.

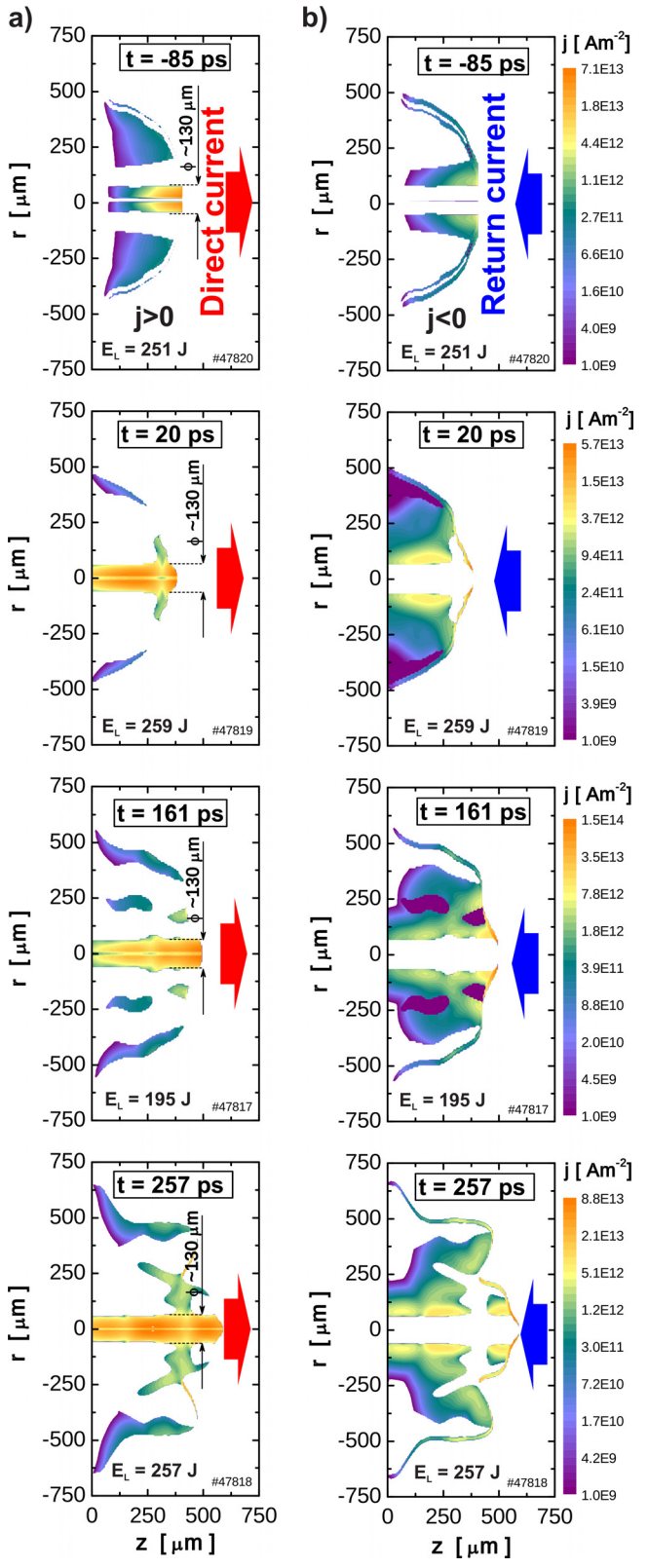

FIG. 4. The current density calculations: distributions of (a) the direct current density and (b) the return current density for the selected time moments corresponding to Fig. 2.

The magnetic field increases in a cylinder of ≈130 μm in diameter, where the current density is positive, and decreases outside the cylinder, where the current density is negative. The electron flux corresponding to a direct current $j \sim 0.5$–1×10^{14} A/m^2 is $n_e v = j/e \sim 3$–6×10^{28} cm^{-2} s^{-1}. This value considerably exceeds that for the flow of thermal electrons. Indeed, in the low-density region of the plasma torch, practically all the energy is contained in the kinetic energy of the plasma particles. Then, knowing that the inverse-bremsstrahlung absorption of laser radiation occurs near the critical plasma density, at a laser intensity of 10^{16} W/cm^2, the estimate for the thermal electron velocity is about 7×10^7 cm/s. Then for the densities in the range of measured values $n_e = 10^{18}$–4×10^{19} cm^{-3}, the thermal electron flux varies in the range from 3×10^{26} to 7×10^{25} cm^{-2} s^{-1}. Thus, the current corresponding to the generation of a measured magnetic field with an amplitude exceeding 10 MG is formed by electrons whose flux is 2–3 orders of magnitude higher than the flux of thermal electrons of an expanding plasma. This is an important experimental indication that this current is formed by the fast electrons. It is supported by the results of previous experiments at PALS performed under similar conditions and by the data of numerical simulation related to these experiments. The fast-electron spectra measured in Ref. 27 had a characteristic energy of about 100 keV. Studies of shock wave generation in experiments[20,30] using first and third harmonic radiation showed that at an intensity of the first harmonic radiation of 0.5–1 $\times 10^{16}$ W/cm^2, up to 6% of the laser energy is transformed into fast-electron energy with an average particle energy of 50–100 keV due to resonant absorption. For the energy of fast electrons of 70 keV and the degree of transformation of laser energy into the fast electron energy of 5 %, we obtain for the fast electron flux the value of 4.5×10^{28} cm^{-2} s^{-1}, the density of electrons in this flux is about 3×10^{18} cm^{-3}. In Sec. III, the detailed analysis is presented particularly for the conditions of the considered experiment.

B. Integral direct and return currents

The total direct and return current along the z-axis are defined as

$$I_z(z) = 2\pi \int_0^{\infty} j_z(r,z) r dr, \qquad (2)$$

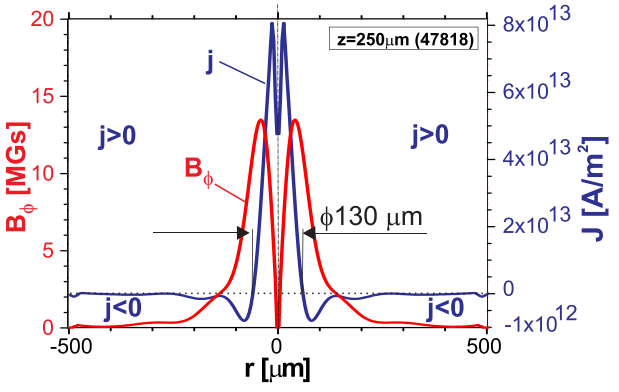

FIG. 5. An example of the radial magnetic field and the current density profiles at $t = 257$ ps (see Fig. 4).

where $j_z(r,z)$ corresponds to either the direct or return current. The results of these calculations, shown in Fig. 6, demonstrate that the integrated direct current is almost the same as the integrated return current, which is obvious for the compact magnetic field distribution. The difference may indicate the input of fast electrons, escaping from the plasma torch, but the reduced plasma density does not allow measuring the magnetic field there. In these peripheral areas, the sensitivity of the polar-interferometer is too small to record both the shift of the interferometric fringes in the inteferomeric channel and the distributions of the Faraday rotation angle in the polarimetric channel. Note that the errors bars for the differences appear to be much larger than differences themselves, which allows only the qualitative estimation for the fast electron current flux. However, as Figs. 6 and 4 show, the main part of the electron current returns back on the plasma periphery. Figure 6 confirms that the total direct current flows within the thin cylinder (with a diameter of about 130 μm) along the plasma torch axis. Figure 6 also shows that both direct and return integral currents $I_z(z)$ have an increasing trend with the distance from the target and

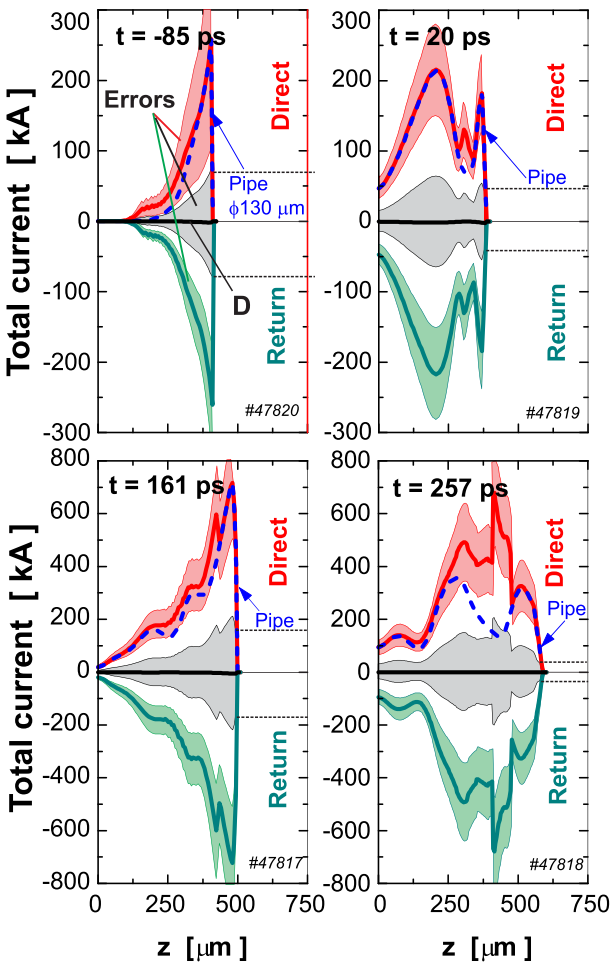

FIG. 6. The total (integrated) direct and return current distributions for the selected times of the plasma expansion. The black solid line D is the difference between the direct and the return currents. The shadows around each curve indicate the errors of the calculated currents, which were estimated from the experimental errors of the polaro-interferometry measurements. The dashed lines at front of the plasma (to the right) indicate a rough estimate for the current of the fast electrons, which can escape the plasma torch.

with the expansion time. This probably should be attributed to the return currents in the plasma in the considered cylindrical region, which cannot be separated from the direct currents in Eq. (1). The maximum absolute value obtained for the direct and return I_z, about 700 kA, is located at the front of the ablative plasma close to the end of the laser pulse (see the diagram in Fig. 6 for $t = 161$ ps). Since the pipe-type collimation is observed up to the end of the laser pulse, we may conclude that the SMF self-consistently directs the laser-accelerated electrons.

C. Energy of the SMF

The spatial SMF energy distribution was calculated using the relation

$$E_B(z) = 2\pi \int_0^{\infty} \frac{B^2(r,z)}{2\mu_0} r dr \ \ \mathrm{J/m}. \tag{3}$$

Figure 7 shows the calculated SMF energy per unit length in the plasma torch.

The total SMF energy in the plasma, defined as $E_{BT} = \int E_B(z)dz$, is depicted in Fig. 8 for selected times during the interaction process. Figure 8 also presents the laser energy E_L, delivered to the target up to the given time. SMF

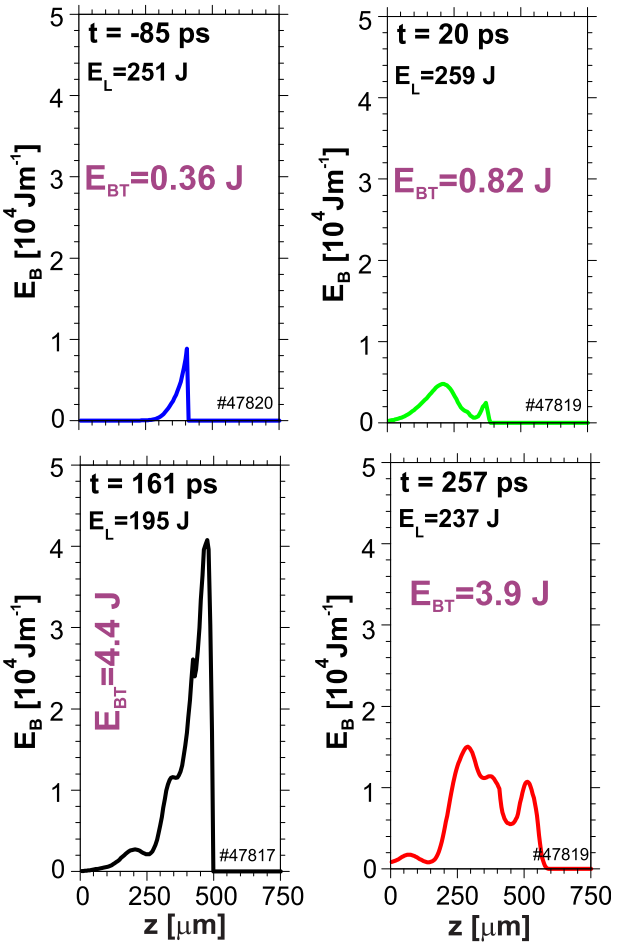

FIG. 7. The integrated energy in the SMF as a function of the distance z from the target calculated using Eq. (3) for selected times.

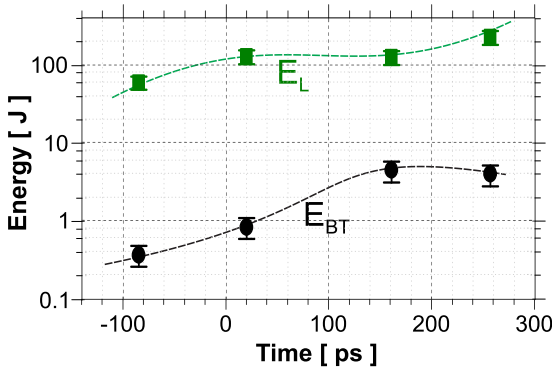

FIG. 8. Temporal evolution of the total SMF energy E_{BT} and the laser energy E_L delivered into the target.

energy reaches the maximum at time $t = 161$ ps when containing approximately 2% of the total laser pulse energy.

III. DISCUSSION

This section is devoted to the magnetization process of the ablative plasma, which is the key point of the current study. The analysis presented below shows that the observed SMF distributions in Fig. 2 are formed mainly due to the kinetics of the fast electrons, though in general it is a competition of the two main mechanisms of field generation, namely, the thermo-electric currents and the fast electron currents (including both the direct and the return currents, see Fig. 4).

Now, consider the theoretical predictions for the magnetic field generation, based on the numerical modeling of plasma hydrodynamical evolution in the conditions of the experiment. It was performed with the Lagrangian hydrodynamic code,[31] which includes refraction of the laser radiation in the axially symmetrical plasma corona, bremsstrahlung, and resonant absorption mechanisms. The later plays a decisive role in the conditions of the experiment, and it is responsible for the generation of the fast electrons. The energy of the fast electrons in the code was defined as an oscillatory energy in the resonantly amplified field. Energy losses of the fast electrons in the target bulk were calculated as the ionization losses for an average ionization potential. Energy losses corresponding to the plasma self-radiation were not directly calculated in the code, but to account for this channel of losses, the laser energy of the incident pulse was decreased two times and simultaneously the electric field in the resonance was multiplied by a factor of $\sqrt{2}$, restoring the correspondence to the real incident pulse.

Note, that the laser focal spot size on the target is much larger than the size of caustic, which is only several wavelengths for a diffraction divergency. Thus, the focal plane was set under the target surface. In this case, the beam direction runs over a range of incident angles from zeroth to a maximum. Another important issue is that actually the irradiated plasma profile is an expanding plasma torch and so is not flat; then the direction of the density gradient changes along the distance from the symmetry axis. In this case, even a plane wave would have different incident angles. Also note, that in our axisymmetrical simulation we considered a circular polarization, dealing with the fact, that the integration over the axial angle of the resonant absorption rate does not depend on the polarization, since the angular dependence is square cosine, which gives 1/2 on average.

As the value of the incident energy flux is relatively high, it deformed the plasma density profile by the ponderomotive action. With the density profile deformation, the size of the plasma inhomogeneities L near the critical surface drops down to the level of the laser wavelength, i.e., to the value smaller than the hydrodynamic spatial scale. For correct calculation of the field amplitude in this case, the model of dissipative structure of the plasma flow near the critical density under the action of the ponderomotive potential of the resonance field[32] was used. Contribution of the resonance absorption depends on the incidence angles of the laser rays, i.e., on their deviation from the optimum angle. This optimum angle corresponds to the value of the parameter $\tau = (k_0 L)^{1/3} \sin\theta_0 = 0.7$,[33] where k_0 is a wave number of the laser radiation and θ_0 is the angle of incidence. During the 2D plasma expansion, the incidence angle is determined by a value of dielectric permeability at the point of the beam reflection (r^*, z^*): $\sin\theta_0 = [\varepsilon(r^*, z^*)]^{1/2}$. When the incidence angle differs from the optimum one, the efficiency of the resonance absorption decreases. If the radiation is fully p-polarized and if it strikes the target at the optimum angle, the resonance absorption efficiency is on the level of 50%.[34] The calculations assume a Gaussian laser beam impacting the target surface in the characteristic focal spot radius R_L. Geometrically, the angle of the beam incidence for $r = R_L$ is approximately 13°. In the case of axially symmetric irradiation by a linearly-polarized laser beam, only half of it becomes p-polarized, whereas the second half impinges with s-polarization. Even if all rays of the laser beam strike the target at the optimum angle, the resonance absorption efficiency cannot be larger than 25%. As the rays are incident at different angles, the total efficiency of the resonance absorption is significantly lower than 25%.[34]

Figure 9 shows the plasma density [Fig. 9(a)] and temperature [Fig. 9(b)] distributions in the plasma torch, obtained in the simulation at the time moments, corresponding to the experimental data. The density distribution ρ is plotted in the mass density (g/cm^3) units, which are standard units for hydrodynamic equations, and, for convenience, the same values are presented in recalculated units of the electron density according to the average ion charge (in cm^{-3}). The mass density and the experimentally obtained electron density n_e, are related by $n_e = \rho Z/Am_p$ (Z and A are the average charge and atomic number of plasma ions, and m_p is the proton mass), which gives $Z = 27$ and $n_e = 2.6 \times 10^{23}\rho$. With this rescaling, the two distributions (the experimental in Fig. 3 and the calculated in Fig. 9) demonstrate a good general agreement in the experimentally achievable region. The calculated distributions, however, are performed for the whole space from the solid target to very small densities, while the experimental range is limited by undercritical plasma densities and resolution. So, experimental distributions (Fig. 3) cover only the range 4×10^{19}–10^{18} cm^{-3}, which corresponds with the given ionization states $Z = 27$ to mass densities in the range $\sim 1.6 \times 10^{-4}$–4×10^{-6} g/cm^3

compared to the values in Fig. 9(a). At the first time moment (−90 ps) in numerical data, the region corresponding to experimental data does not have a sufficient resolution. At the second time moment (30 ps), one can compare, i.e., the experimental density at a distance along the z-axis 380 μm, which is 2×10^{18} cm^{-3}, with plasma density in simulation 8×10^{-6} g/cm^3, which rescales to $n_e = 2.1 \times 10^{18}$ cm^{-3}. At the last time moment (270 ps), the similar comparison at a distance 700 μm the experimental electron density is 10^{18} cm^{-3}, while the plasma density in simulations is 4×10^{-6} g/cm^3, which corresponds to $n_e = 1.05 \times 10^{18}$ cm^{-3}. Note, that in the density region $4 \times 10^{19} \ldots 10^{18}$ cm^{-3} the experimental data shows a higher value of the density gradients, which at late times even acquires a concave shape in the central direction. These features are not reproduced in the numerical simulations, and are likely related to the effect of the plasma magnetization due to the fast electron currents.

The calculated temperature distributions have a natural maximum near the critical density. Time dependence of the maximum temperature follows the laser intensity. At the time moment near the maximum laser intensity (30 ps), temperature maximum is about 3.4 keV, and at time moments of increase and decrease of the laser pulse intensity (−90 and 150 ps), temperature maxima are about 2.5 keV. At the moment of 270 ps, which is 20 ps after the end of the laser pulse, the temperature value at maximum is only 1 keV. Simulation results evidently demonstrate isothermal plasma expansion with undercritical density; the spatial temperature distributions in the experimentally accessible region are almost homogeneous. At the time moments of 30, 150, and 270 ps, the plasma temperatures in this region are 2.8 keV, 2 keV, and 1 keV, respectively. The calculated energy of the thermal electrons with the density in the range 4×10^{19}–10^{18} cm^{-3}, which corresponds to the experimental measurements, is 0.1 J for the time moment of 150 ps and 0.06 J for 270 ps. The radial plasma size in the numerical simulations is less than that in the experimental data and approaches the later (reaching 500 μm) at the fourth time moment (270 ps). This is due to the laser pulse profile, which additionally heated the target out of the ideal (gaussian with the size of 50 μm) focal spot size, used in the simulations.

To distinguish between the different magnetic field sources, namely the thermocurrent and the fast electron currents, we first estimate the magnetic field values by the hydrodynamic approach without kinetic effects, and then refer to the electron currents (both the direct and the return, see Fig. 4).

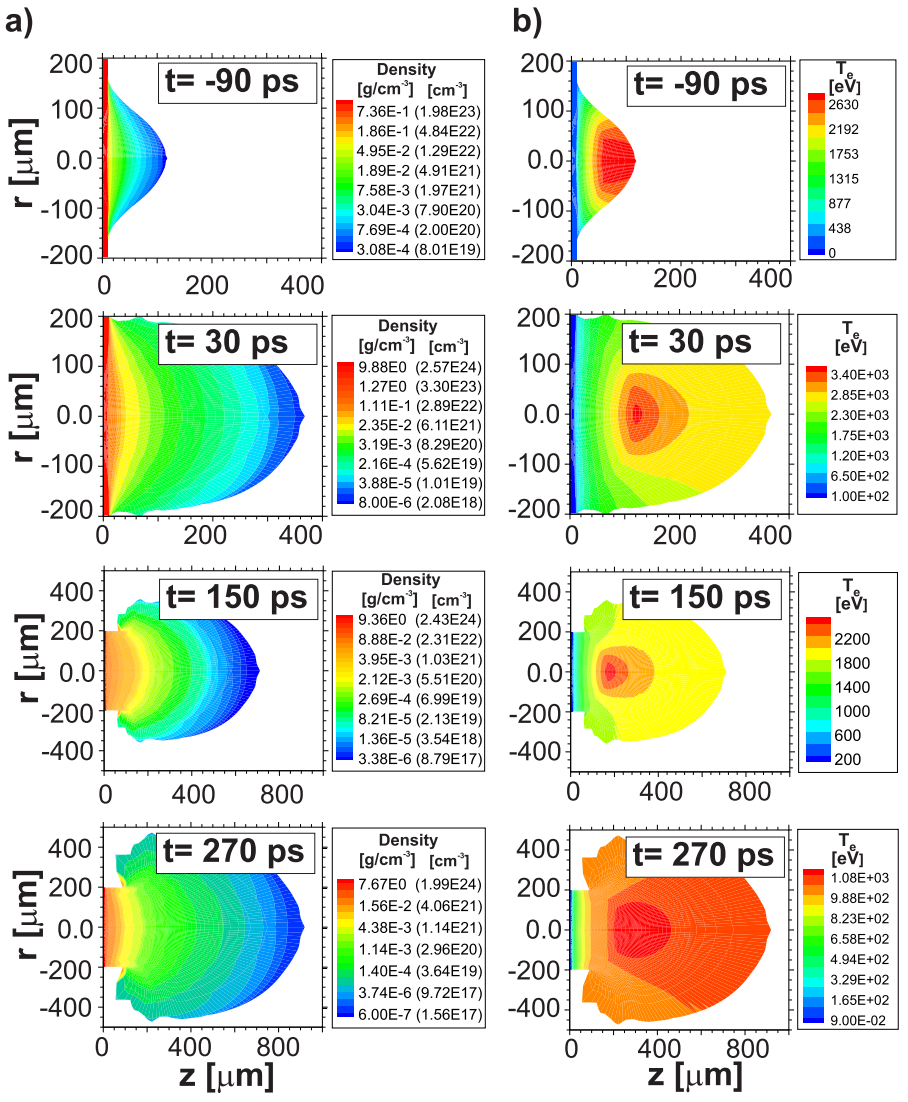

FIG. 9. Results of the 2 D numerical modeling of the massive planar Cu target irradiated by the laser pulse of the same parameters, as in the experiment: (a) electron density and (b) temperature distributions.

To extract the SMF generation due to the thermo-current mechanism defined by a crossing gradients $\nabla n_e \times \nabla T_e$, an additional module was introduced in the hydrodynamic code. This module calculates the density and temperature gradients at each time step using the spatial distributions of the density $n_e(r,z)$ and the temperature $T_e(r,z)$, see Fig. 9.

Based on this data, the spatial distribution of the time derivative $\frac{dB}{dt} = -\frac{c}{en_e}\nabla n_e \times \nabla T_e$ (c is the speed of light and e is the electron charge) was found (hereafter we omit index ϕ for the magnetic field, so that $B_\phi(r,z) \equiv B(r,z)$). The time derivative $\frac{dB}{dt}$ is shown in Fig. 10(a). Integration of $\frac{dB}{dt}$ in time is performed in Lagrangian coordinates, so that the full time derivative reads $\frac{d}{dt} = \frac{\partial}{\partial t} + \vec{v}\nabla$ which allows to take into account the field convection. Although the full set of magnetohydrodynamic equations is not resolved in this scheme, it nevertheless gives the correct estimate for the magnetic field, produced by the $\nabla n_e \times \nabla T_e$ mechanism. To substantiate this statement, we remind a single-liquid hydrodynamic Eq. (13) in Ref. 23. The estimations of different terms, presented in Ref. 23, showed, that the thermocurrent source plays a major role in the conditions of this experimental setup

$$\frac{\partial\langle\vec{B}\rangle}{\partial t} + \frac{c^2}{4\pi}\nabla \times \frac{\nabla \times \langle\vec{B}\rangle}{\sigma} - \nabla \times (\vec{v} \times \langle\vec{B}\rangle) - \frac{c}{e}\nabla \times \frac{\nabla p + \vec{R}_T}{n_e} - \frac{cm_e}{e}\nabla \times \frac{d\vec{v}}{dt} \approx 0, \tag{4}$$

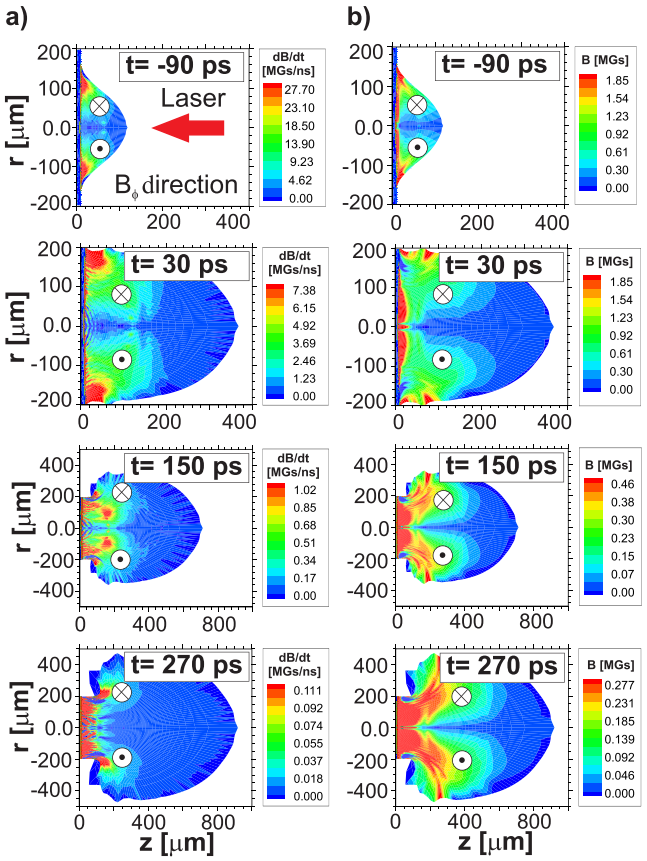

FIG. 10. Results of the 2 D numerical modeling of the massive planar Cu target irradiated by the laser pulse of the same parameters, as in the experiment: (a) $\frac{dB}{dt} = -\frac{c}{en_e}\nabla n_e \times \nabla T_e$ and (b) the SMF distributions obtained by integration of the time derivative $\frac{dB}{dt}$.

where $\langle\vec{B}\rangle$ is the average magnetic field, and $\vec{v} = \langle\vec{V}\rangle$ is the average plasma flow velocity. For the qualitative estimation for the magnetic field, it is enough to leave the source term [the fourth one in Eq. (4)], and to rewrite the convective term [the third one in Eq. (4)]

$$\nabla \times \left(\vec{v} \times \langle\vec{B}\rangle\right) = -(\vec{v}\nabla)\langle\vec{B}\rangle - \langle\vec{B}\rangle(\nabla\vec{v}) + \left(\langle\vec{B}\rangle\nabla\right)\vec{v},$$

where: $(\langle\vec{B}\rangle\nabla)\vec{v} \approx 0$ because of the geometrical orientation of the magnetic field (azimuthal symmetry). Using the continuity equation we see that $\langle\vec{B}\rangle(\nabla\vec{v}) = \langle\vec{B}\rangle\frac{d(\ln n_e)}{dt}$ is a slowly varying function. Then qualitatively

$$\frac{\partial\langle\vec{B}\rangle}{\partial t} + (\vec{v}\nabla)\langle\vec{B}\rangle = \frac{\partial\langle\vec{B}\rangle}{\partial t} \approx \frac{c}{e}\nabla \times \frac{\nabla p}{n_e}, \tag{5}$$

where: $\vec{R}_T$ occurring in Eq. (4) is omitted within the considered accuracy, taking into account that the temperature gradients are small in the highly magnetized region inside the plasma torch (see Fig. 2), as described above.

The integrated magnetic field component is shown at the selected times in Fig. 10(b). The spatial distribution of the magnetic field differs from the experimental observation shown in Fig. 2. While in Fig. 2, the maximum magnetic field is close to the axis of the plasma torch, in Fig. 10(b) the magnetic field increases out from the axis, i.e., for large distances r, due to the magnetic source properties and convection. Besides, the maximal values of the magnetic field, generated by the thermocurrents, more than an order less, than those registered in the experiment. The difference between the density gradients and the front shape of the expanding plasma in the theoretical simulations and the experimental data, noted above, take place in the low-density region, where thermocurrents are not high enough to generate the magnetic field efficiently, see the regions in Fig. 10. In the important high-density plasma region, the gradients of the electron density and the temperature in simulation are only slightly greater than the experimental values due to smaller torch radius, as discussed above. So, the calculated magnetic field values, originated from thermocurrents, may be considered as upper values [Fig. 10(b)]. This proves, that the thermocurrents cannot explain the experimental values of the magnetic field of the 10–30 MG level.

The observed difference may be explained by the kinetics of the fast electrons, which do not explicitly act as a magnetic field source in the used numerical scheme. However, several important characteristics calculated within the hydrodynamic code provide a possibility to estimate the source kinetics and the corresponding magnetic field amplitude. In the calculation scheme, the maximum energy of the fast electrons is defined for an optimal incident angle, as described in Ref. 32. The average fast electron energy was approximated as a half of the maximum fast electron energy. Fast electrons are present in the simulations only during the laser pulse action, so the latest moment, $t = 270$ ps, is omitted in the estimation.

Table I shows the fraction of the laser energy corresponding to the resonance absorption (δ_{ar}), average fast electron energy (ϵ_h), average fast electron velocity (v_h), and

TABLE I. Fast electron characteristics obtained in 2D numerical simulations at the different moments of copper target irradiation with the PALS-laser beam.

Time (ps)	Fraction of laser energy absorbed by the resonance mechanism δ_{ar}	Incident laser power $Q_{in}, 10^{12}$ (W)	Characteristic energy of fast electrons $\epsilon_h = \epsilon_{h\,max}/2$ (keV)	Power absorbed in fast electrons $Q_{ar}, 10^{12}$ (W)	Characteristic velocity of fast electrons v_h(cm/s)
–90	0.0270	0.6977	58	0.0188	1.317×10^{10}
30	0.0555	1.0000	72	0.0555	1.443×10^{10}
150	0.0579	0.2442	55	0.0141	1.289×10^{10}

incident laser energy flux (Q_{in}), absorbed in fast electrons energy flux (Q_{ar}). Table II presents at different time moments the estimates for average fast electron density n_h in the central channel with the radius, equal to the laser beam radius r_0, average density of the fast electron current j_h, and average value of the magnetic field B_h, generated by the fast electrons, as well as the current density and the magnetic field amplitudes, registered in the experiment. The estimates in the Table II were performed with the numbers from Table I by the following expressions:

$$n_h = \frac{Q_{ar}}{\pi r_0^2 \varepsilon_h v_h}, \tag{6a}$$

$$j_h = e n_h v_h, \tag{6b}$$

$$B = \frac{2eQ_{ar}}{c r_0 \varepsilon_h}. \tag{6c}$$

Agreement between the theoretical and experimental numbers of Table II shows that the magnetic fields of the 10–30 MG scale, registered in the experiment at PALS, are produced by the current of the fast electrons, generated due to the resonant absorption mechanism. Note, that the fast electron current of 300–800 kA, corresponding to the current density of $3–10 \times 10^{13}$ A/m^2, see Table II, exceeds the Alfven limit of 17 kA for the current of non-relativistic electrons. This fact may be explained by the presence of additional electrostatic tension in the plasma torch, which was not measured in the experiment.

An important conclusion could be obtained from the comparison between the energy of the magnetic field and the energy of the fast electrons which form the electric current. We note that for a coil-type electron current in a stationary regime, the magnetic field energy may be scaled as $E_{BT} \sim \frac{LI^2}{2}$, where L is an inductance and I is the total current for the given magnetic field. For our fountain-like geometry $L \sim \mu\mu_0 r/4$, where μ is the magnetic permeability, $r \sim 500\,\mu$m is the characteristic radius of the SMF distribution, $I \sim \pi r_0^2 \times e n_h v_h$, and $r_0 \sim 50\,\mu$m is the characteristic radius of the current distribution (pipe radius in Fig. 4). Energy of the electrons which form the electric current (hot, or fast electrons) scales as $E_{hc} \sim z_0 \pi r_0^2 \times n_h m_e v_h^2/2$, where $z_0 \sim 500\,\mu$m is a characteristic length of the SMF and electric current distributions. Then,

$$E_{BT} \sim \mu\alpha E_{hc}, \quad \alpha = \mu_0 r \frac{n_h e^2 \pi r_0^2}{4 z_0 m_e} \sim 280.$$

Note that the energy E_{hc} is the energy of the fast electrons, which are moving in the cylinder of radius r_0 during the time z_0/v_h, and for the corresponding estimate we use $n_h \approx 4 \times 10^{18}$ cm^{-3}, $\varepsilon_h \approx 70$ keV, see Tables I and II. For instance, at the third time moment (30 ps, approximately in the middle of the pulse) one can find $E_{hc} \sim 0.11$ J, though the total energy, which was absorbed by the fast electrons up to the time moment t, is much more: $E_h \sim E_{hc} t v_h / z_0$, which reads ≈7.7 J at the end of the pulse. The composed dimensionless parameter $\mu\alpha$ describes the equilibrium energy balance in a "coil", created by fast electrons in the plasma torch. It depends on the structure of the current - if it contains ions, it would have a much less value because of the heavier masses. From the numbers above the magnetic permeability may be estimated as $\mu \sim 0.14 \ll 1$, which emphasizes the diamagnetic properties of the plasmas. Indeed, the fast electrons play the role of the external magnetization source. Due to plasma diamagnetism, the return currents in the plasma volume are induced by acceleration of thermal electrons. They can more easily maintain the plasma electroneutrality than the fast electrons, since their Debye length is much smaller. The result of this thermal electron flow is clearly seen in Fig. 6: the integrated currents would have a constant value along the z-axis without the

TABLE II. Average densities of the fast electron flow and current as well as average magnetic field due to fast electron current estimated on the basis of 2 D numerical simulation data together with the magnetic field amplitude measured in the experiment and current density amplitude recalculated on the basis of polaro-interferometric measurements.

Time (ps)	Average density of the fast electrons (theory) 10^{18} (cm^{-3})	Average density of the fast electrons current (theory) 10^{13} (A/m^2)	Current density amplitude (experiment) 10^{13} (A/m^2)	Average magnetic field due to the fast electrons (theory) [MG]	Magnetic field amplitude (experiment) [MG]
–90	1.9	3.9	5.7	12.9	10
30	4.5	9.8	15	30.8	28
150	1.5	3.1	8.8	10.3	16

return currents. As a result of this, the maximum values of the SMF are in a good agreement between the experimental data and the calculated numerical results only at the front of the plasma torch, where these return currents are small. To the left of the region of the peak direct current in Fig. 6, the shown curve indicates actually an integrated current which increases to the left (in average) part of the directed return current in the central region. The magnetic field in the torch volume, therefore, is weaker, and the magnetic field energy is less so there would be no appearance of return currents. Note that this is a simple estimation, which does not take into account any time-dependence, plasma structure, other magnetization mechanisms, experimental errors, and other factors. It just explicates how the magnetization of the plasma torch may be related to the fast electron current.

IV. CONCLUSIONS

Our combined analysis of the highly resolved experimental data reveals the nature of the magnetic field generation in the situation, when the intense sub-relativistic laser pulse irradiates a massive target. It is shown that the fast electrons are of crucial importance for the formation of the magnetic fields, whose distribution was directly observed in the experiment. This key feature is consistent with the analysis of currents and energies of the fast electrons derived from the experimental data. However, most of the fast electrons are not fast enough to escape from the plasma plume. Only a fraction of the fast electrons responsible for the magnetic field distribution observed in the central part of the plasma plume can overcome the charge-separation potential created by slow ions. This condition of quasi-neutrality is normally satisfied for the time scales of a few tenths of picoseconds or even less in the laser-driven plasmas.

The highly-resolved SMF distributions were measured using femtosecond polaro-interferometry. A successful application of the novel technique proves the usefulness of this unique tool for laser plasma research. We have also demonstrated that the SMF distributions may be used for measurements of the current distribution in the plasma corona. Based on this approach, we found that the plasma magnetization in the sub-relativistic regime results from the kinetic processes related to the fast electrons in the plasma corona. The kinetic magnetization is quite effective in the considered region of parameters and gives the magnetic field values of about an order higher than the $\nabla n_e \times \nabla T_e$ mechanism. The understanding of the physics of the SMF generation is very important for many problems related to the astrophysical magnetized plasma, ablative plasma behaviour, fast electron generation, etc. The generated fast electron currents may effectively magnetize ablative plasma, which in turn collimate the fast electron flow. The detailed understanding of these effects may help to produce jets of magnetized plasma with the desired characteristics, optimize capacitor-coil targets, generate tailored fluxes of fast electrons or contribute to the development of particle laser-based acceleration schemes.

ACKNOWLEDGMENTS

This paper was supported by the Access to the PALS RI under the EU LASERLAB IV project (Grant Agreement No. 654148), by the Ministry of Science and Higher Education, Republic of Poland (Decision no. 3554/H2020/2016/2), by the Ministry of Education, Youth and Sports of the Czech Republic, Grant No.: LM2015083 (PALS RI) and the ELI: Extreme Light Infrastructure Project No. CZ.02.1.01/0.0/0.0/15008/0000162, and by the Czech Science Foundation, Project No. P205/11/P712. The work of S. Gus'kov and N. Demchenko was supported by the Russian Foundation for Basic Research Project Nos. 17-02-00059- and 17-02-00021- and the work of Ph. Korneev was supported by RFBR 16-52-50019-JF. This work was also supported by the Program of Increase in the Competitiveness of the National Research Nuclear University MEPhI (Contract No. 02.a03.21.0005, 27.08.2013). This work has also been carried out within the framework of the EUROfusion Consortium and received the funding from the Euratom research and training programme 2014-2018 under Grant Agreement No 633053 (Project No. AWP15-ENR-01/CEA-02). The views and opinions expressed herein do not necessarily reflect those of the European Commission. We are thankful to V. Tikhonchuk for productive discussions.

[1]W. J. Hogan, *Energy from Inertial Fusion*, edited by W. J. Hogan (IAEA, Vienna, 1995).
[2]S. Atzeni and J. Meyer-ter-Vehn, *The Physics of Inertial Fusion* (Oxford University Press, Oxford, 2004).
[3]J. J. Santos, M. Bailly-Grandvaux, L. Giuffrida, P. Forestier-Colleoni, S. Fujioka, Z. Zhang, P. Korneev, R. Bouillaud, S. Dorard, D. Batani, M. Chevrot, J. E. Cross, R. Crowston, J. L. Dubois, J. Gazave, G. Gregori, E. d'Humies, S. Hulin, K. Ishihara, S. Kojima, E. Loyez, J. R. Marqus, A. Morace, P. Nicola, O. Peyrusse, A. Poy, D. Raffestin, J. Ribolzi, M. Roth, G. Schaumann, F. Serres, V. T. Tikhonchuk, P. Vacar, and N. Woolsey, "Laser-driven platform for generation and characterization of strong quasi-static magnetic elds," New J. Phys. **17**, 083051 (2015).
[4]H. Shiraga, H. Nagatomo, W. Theobald, A. A. Solodov, and M. Tabak, "Fast ignition integrated experiments and high-gain point design," Nucl. Fusion **54**, 054005 (2014).
[5]N. G. Basov, S. Yu. Gus'kov, and L. P. Feoktistov, J. Sov. Laser Res. **13**, 396 (1992).
[6]M. Tabak, J. Hammer, M. E. Glinsky, W. L. Kruer, S. C. Wilks, J. Woodworth, E. M. Campbell, M. D. Perry, and R. J. Mason, "Ignition and high gain with ultrapowerful lasers," Phys. Plasmas **1**, 1626 (1994).
[7]C. Ren, M. Tzoufras, F. S. Tsung, W. B. Mori, S. Amorini, R. A. Fonseca, L. O. Silva, J. C. Adam, and A. Heron, "Global simulation for laser-driven MeV electrons in fast ignition," Phys. Rev. Lett. **93**, 185004 (2004).
[8]Ph. Korneev, E. d'Humires, and V. Tikhonchuk, "Gigagauss-scale quasi-static magnetic field generation in a snail-shaped target," Phys. Rev. E **91**(4), 043107 (2015).
[9]Ph. Korneev, V. Tikhonchuk, and E. dHumires, "Magnetization of laser-produced plasma in a chiral hollow target," New J. Phys. **19**, 033023 (2017).
[10]S. Yu. Gus'kov and F. A. Korneev, "Neutronless nuclear reaction at inertial confinement of the magnetized plasma of laser-accelerated protons and boron nuclei," JETP Lett. **104**, 1–5 (2016).
[11]C. A. Walsh, J. P. Chittenden, K. McGlinchey, N. P. L. Niasse, and B. D. Appelbe, "Self-generated magnetic fields in the stagnation phase of indirect-drive implosions on the National Ignition Facility," Phys. Rev. Lett. **118**, 155001 (2017).
[12]D. D. Ryutov, R. P. Drake, and B. A. Remington, "Criteria for scaled laboratory simulations of astrophysical MHD phenomena," Astrophys. J. Suppl. Ser. **127**(2), 465–468 (2000).
[13]J. A. Stamper, K. Papadopoulos, R. N. Sudan, S. O. Dean, E. A. McLean, and J. M. Dawson, "Spontaneous magnetic fields in laser-produced plasmas," Phys. Rev. Lett. **26**, 1012 (1971).

[14]L. Biermann, Z. Naturforsch. **5A**, 65 (1950).
[15]N. G. Basov, J. Wolowski, E. G. Gamali, S. Denus, T. Pisarczyk, A. A. Rupasov, G. S. Sarkisov, G. B. Sklizkov, V. T. Tikhonchuk, and A. S. Shikanov, "Detection of spontaneous magnetic-fields in a laser plasma in the 'Delfin-1' device," J. Exp. Theor. Phys. Lett. **45**, 213–217 (1987).
[16]R. N. Sudan, "Mechanism for the generation of 109 G magnetic fields in the interaction of ultraintense short laser pulse with an overdense plasma target," Phys. Rev. Lett. **70**, 3075 (1993).
[17]W. L. Kruer, *The Physics of Laser Plasma Interactions* (Addison-Wesley, New York, 1988).
[18]J. F. Drake, R. G. Kleva, and M. E. Mandt, "Structure of thin current layers: Implications for magnetic reconnection," Phys. Rev. Lett. **73**, 1251 (1994).
[19]J. A. Stamper, "Review on spontaneous magnetic fields in laser-produced plasmas: Phenomena and measurements," Laser Part. Beams **9**, 841 (1991).
[20]S. Yu. Gus'kov, N. N. Demchenko, A. Kasperczuk, T. Pisarczyk, Z. Kalinovska, T. Chodukowski, O. Renner, M. Smid, E. Krousky, M. Pfeifer, J. Skala, J. Ullschmiad, and P. Pisarczyk, "Laser-driven ablation through fast electrons in PALS-experiment at the laser radiation intensity of 150 P W/cm^2," Laser Part. Beams **32**, 177 (2014).
[21]T. Pisarczyk, S. Yu. Gus'kov, Z. Kalinowska, J. Badziak, D. Batani, L. Antonelli, G. Folpini, Y. Maheut, F. Baffigi, S. Borodziuk, T. Chodukowski, G. Cristoforetti, N. N. Demchenko, L. A. Gizzi, A. Kasperczuk, P. Koester, E. Krousky, L. Labate, P. Parys, M. Pfeifer, O. Renner, M. Smid, M. Rosinski, J. Skala, R. Dudzak, J. Ullschmied, and P. Pisarczyk, "Pre-plasma effect on energy transfer from laser beam to shock wave generated in solid target," Phys. Plasmas **21**, 012708 (2014).
[22]T. Pisarczyk, A. A. Rupasov, G. S. Sarkisov, and A. S. Shikanov, "Faraday-rotation method for magnetic field diagnostic in a laser plasma," J. Sov. Laser Res. **11**, 1 (1990).
[23]T. Pisarczyk, S. Yu. Gus'kov, R. Dudzak, T. Chodukowski, J. Dostal, N. N. Demchenko, Ph. Korneev, Z. Kalinowska, M. Kalal, O. Renner, M. Smid, S. Borodziuk, E. Krousky, J. Ullschmied, J. Hrebicek, T. Medrik, J. Golasowski, M. Pfeifer, J. Skala, and P. Pisarczyk, "Space-time resolved measurements of spontaneous magnetic fields in laser-produced plasma," Phys. Plasmas **22**, 102706 (2015).
[24]J. Dostal, R. Dudzak, T. Pisarczyk, M. Pfeifer, J. Huynh, T. Chodukowski, Z. Kalinowska, E. Krousky, J. Skala, J. Hrebicek, T. Medrik, J. Golasowski, L. Juha, and J. Ullschmied, "Synchronizing single-shot high-energy iodine photodissociation laser PALS and high-repetition-rate femtosecond Ti: Sapphire laser system," Rev. Sci. Instrum. **88**, 045109 (2017).
[25]I. Ghozeil, "Hartmann and other screen tests," in *Optical Shop Testing*, edited by D. Malacara (Wiley, New York, 1992), pp. 367–396.
[26]J. Cikhardt, J. Krsa, M. De. Marco, M. Pfeifer, A. Velyhan, E. Krousk, B. Cikhardtov, D. Klr, K. ez, J. Ullschmied, J. Skla, P. Kube, and J. Kravrik, "Measurement of the target current by inductive probe during laser interaction on terawatt laser system PALS," Rev. Sci. Instrum. **85**, 103507 (2014).
[27]S. Singh, H. Ahmed, R. Dudzak, J. Dostal, T. Chodukowski, L. Giuffrida, P. Hadjisolomu, T. Hodge, J. Hrebicek, L. Juha, Z. Kalinowska, E. Krousky, M. Krus, P. Lutoslawski, M. De. Marco, M. Pfeifer, J. Skala, J. Ullschmeid, T. Pisarczyk, M. Borghesi, D. Kumar, and S. Kar, "Magnetic field generation from a foil-coil target using kJ – ns class lasers," in Proceedings of the 43nd EPS Conference on Plasma Physics, Leuven, Belgium, 4–8th June 2016, p. P2.102.
[28]M. G. Drouet and H. Pépin, "Parametric study of the current induced in a CO2 laser plasma," Appl. Phys. Lett. **28**, 426 (1976).
[29]M. G. Drouet and R. Bolton, "Distribution of self-generated current in laser-produced plasmas," Phys. Rev. Lett. **36**, 591 (1976).
[30]T. Pisarczyk, S. Yu. Gus'kov, O. Renner, N. N. Demchenko, Z. Kalinowska, T. Chodukowski, M. Rosinski, P. Parys, M. Smid, J. Dostal, J. Badziak, D. Batani, L. Volpe, E. Krousky, R. Dudzak, J. Ullschmied, H. Turcicova, J. Hrebicek, T. Medrik, M. Pfeifer, J. Skala, A. Zaras-Szydlowska, L. Antonelli, Y. Maheut, S. Borodziuk, A. Kasperczuk, and P. Pisarczyk, "Pre-plasma effect on laser beam energy transfer to a dense target under conditions relevant to shock ignition," Laser Part. Beams **33**, 221–236 (2015).
[31]I. G. Lebo, N. N. Demchenko, A. B. Iskakov, J. Limpouch, V. B. Rozanov, and V. F. Tishkin, "Simulation of high-intensity laser-plasma interactions by use of the 2D Lagrangian code ATLANT-HE," Laser Part. Beams **22**, 267–273 (2004).
[32]S. Yu. Gus'kov, N. N. Demchenko, K. N. Makarov, B. V. Rozanov, Yu. A. Satov, and B. Yu. Sharkov, "Efficiency of generation of highly ionised atoms under resonance absorption of CO2-laser radiation," Quantum Electron. **41**(10), 886 (2011).
[33]V. L. Ginzburg, *The Propagation of Electromagnetic Waves in Plasmas*, edited by J. B. Sykes and R. J. Tayler (Pergamon, London, Addison-Wesley, Reading, MA, 1964) (translated from the Russian Edition).
[34]J. P. Freidberg, R. W. Mitchell, R. L. Morze, and L. I. Rudsinski, "Resonant absorption of laser light by plasma targets," Phys. Rev. Lett. **28**, 795 (1972).